Droplet spindown in a high-temperature gas environment

Jun Xin* and Constantine M. Megaridis
Department of Mechanical Engineering, The University of Illinois at Chicago, Chicago, IL, USA

The spindown and heating of a spherical droplet in an initially undisturbed infinite fluid is investigated by means of a numerical model based on finite-difference discretization techniques. The nonevaporating droplet enters the hot gas while rotating about a diameter and has no translational motion with respect to the suspending medium. Special attention is given to the transient secondary (nonrotational) motion developed as a result of shear interaction between the two phases. The results indicate that for droplet sizes and rotation frequencies representative of droplet combustion applications; i.e., Reynolds $\sim O(0.1)$, the secondary motion in both phases remains weak and heat transport is conduction-dominated. On the other hand, the secondary motion is strengthened with increased values of the rotational Reynolds number. The characteristic time for droplet spindown is found to be proportional to the square of the droplet radius. The results also show that the rotational deceleration time is of the same order of magnitude with the translational response time of the droplet. Finally, the thermocapillary stress effects on fluid dynamics and heat transfer are investigated in this flow configuration. *© 1996 by Elsevier Science Inc.*

Keywords: droplet rotation; spindown; transient heating; thermocapillary flow

Introduction

Droplet phenomena are pertinent to a wide variety of physical processes ranging from atmospheric transport of rain droplets to spray cooling and liquid fuel evaporation and combustion. A significant percentage of former investigations involves situations where the droplets are quiescent or have a relative translational velocity with respect to the surrounding medium. On the other hand, a relatively small number of studies has concentrated on rotating droplet configurations. In spray applications, either because of the atomizer design and/or the highly turbulent ambient flow, the droplets may also acquire an angular velocity about their own axis. Considering that most practical flows are turbulent and feature high levels of fluctuating vorticity (Tennekes and Lumley 1972), it is important to evaluate the role of droplet rotation in the internal transport processes and, eventually, in droplet gasification.

Rotating-sphere flows have been utilized to provide insight on the transport phenomena around a spinning droplet. The ambient flow induced by a rotating sphere—which possesses a uniform angular velocity about a diameter in a fluid at rest—is of intrinsic interest in the fields of meteorology and astrophysics, amongst others, and has received attention theoretically, experimentally, and numerically. The earliest work in this subject dates back to one and one-half centuries ago. Stokes (1845) considered the problem of a slowly rotating sphere with a small Reynolds number ($\mathrm{Re}_g = r_0^2 \Omega \rho_g / \mu_g$) and presented the first approximate theoretical results. For small values of Re_g, better approximations to the solution in terms of powers of Re_g were obtained by Collins (1955), Thomas and Walters (1964), and Takagi (1977). At large values of Re_g, using boundary-layer approximations, the flow engendered by a rotating sphere was investigated theoretically by Howarth (1951), Nigam (1954), Kreith et al. (1963), and Banks (1976). Also by using a series approach, Dennis et al. (1980) determined the steady flow induced by a rotating sphere at low and moderate Reynolds numbers. In another investigation conducted by Dennis et al. (1981), the Navier–Stokes equations were solved numerically by means of a finite-difference method. The steady flow was studied for Reynolds numbers in the range from 1 to 5000.

In all of the above investigations of the ambient flows induced by a rotating sphere, the transients were not considered. Dennis and Ingham (1979) used a series truncation method to investigate the laminar boundary layer on an impulsively started rotating sphere. Finally, experimental studies on the ambient flows induced by a rotating sphere were conducted by Kreith et al. (1963), Kobashi (1957), Sawatzki (1970) and Kohama and Kobayashi (1983).

Megaridis et al. (1994) used a suspended droplet configuration to examine the droplet internal circulation imparted by surface rotation. It was shown that the steady-state motion established from spatially nonuniform surface rotation has a helical character and bears little resemblance to the toroidal internal flows developed within droplets under axisymmetric conditions.

Although the influence of axisymmetric ambient flows on droplet evaporation and combustion rates has been examined in detail (see review articles by Law 1982; Faeth 1983; Sirignano 1983, 1993; Dwyer 1989, and references cited therein), little

---

Address reprint requests to Prof. C. M. Megaridis, Dept. of Mechanical Engineering (M/C 251), University of Illinois at Chicago, 842 W. Taylor St., Chicago IL 60607-7022, USA.

*Currently at the Dept. of Mechanical Engineering, University of Wisconsin, Madison WI 53706, USA.

Received 9 February 1996; accepted 26 June 1996

Int. J. Heat and Fluid Flow 17: 567–578, 1996

655 Avenue of the Americas, New York, NY 10010

0142-727X/96/$15.00
PII S0142-727X(96)00084-8

attention has been paid to the effects of rotation on droplet combustion dynamics. Only until recently and under steady rotating conditions, the influence of spinning on droplet vaporization has been investigated experimentally by Pearlman and Sohrab (1991) and theoretically by Lozinski and Matalon (1992). Both studies concluded that the induced secondary flow in the gas enhances the vaporization rate and shortens the droplet lifetime. From the subsequent analytical results of Lozinski and Matalon (1994), the reduction of a rotating-droplet lifetime with respect to quiescent conditions is given by the factor $(1 - 0.4\,\mathrm{Re}_g^4 \mathrm{Pr}_g^{1.5} C/K)$, where Re_g is the rotational Reynolds number, Pr_g the gaseous Prandtl number, C a correction factor to the burning rate, and K the vaporization constant. In most practical spray systems, the rotational Reynolds number is small; for example, for a 200 μm diameter droplet rotating at 100 Hz in 1 atm and 1000 K air, $\mathrm{Re}_g < 0.1$. According to this formula and because C is also a small quantity, the effect of rotation on the droplet lifetime is very limited.

Hou and Lin (1993) examined the influence of flow rotation on droplet combustion and evaporation using a burning liquid-pool experimental system and a numerical model considering a nonreactive, rotating stagnation point flow. They showed that both convection and diffusion transports are weakened by flow rotation, resulting in the suppression of the evaporation strength of the liquid.

Xin and Megaridis (1996) addressed the droplet/gas interactions in nonisothermal rotating flows using a concentric tube/droplet array configuration. Under the conditions considered in that study, initially quiescent droplets were rotationally accelerated within relatively short time periods compared to their estimated evaporation lifetimes, and the characteristic times for transient heating and spinup were of comparable magnitude. Finally, the effects of rotation on droplet heating were found to be insignificant for small droplets; i.e., 100 μm or smaller, and the corresponding low values of rotational Reynolds numbers.

A typical droplet combustion event starts with liquid heatup, during which vaporization is weak (negligible for low-volatility fuels). Subsequently, vapor buildup and ignition occurs, leading to the stage where vigorous vaporization persists until the end of the droplet lifetime. The liquid heatup period is important, because it determines the initial conditions for the subsequent events. To this end, examination of droplet transient heatup in the absence of evaporation can provide useful insight in droplet combustion. The current study investigates the situation where a rotating nonevaporating spherical droplet is suddenly exposed to a quiescent hot gas. The axis of rotation does not change direction with time, and no translational velocity is assumed between the two phases. After injection, the angular velocity of the rotating droplet decays gradually due to the shear stress on the liquid–gas interface, while the surrounding gas is set into motion through its contact with the decelerating spinning droplet. A description of the flow field in both phases is presented in the paper, and special consideration is given to the energy transport under these circumstances. Finally, the effect of thermocapillary motion along the droplet surface is examined, and its implications on fluid and heat transport are discussed.

Model definition

Figure 1 illustrates the flow configuration for the rotating droplet along with the employed notation. The gaseous medium is assumed to be initially quiescent. Both liquid and gas phases are incompressible with constant thermophysical properties. The flow is assumed to be symmetric about the axis of rotation x, and external body forces are neglected. While a complete treatment of the fluid dynamical and heat transport phenomena is considered in this investigation, liquid evaporation has not been modeled. In that respect, the results of this work are relevant to nonvolatile liquids. However, the effect of rotation on heat transport rates may provide insight to subsequent investigations involving evaporating fuels.

The following mathematical equations govern the fluid and energy transport both in and around the droplet. For the additional steady-state calculations involving a rotating solid sphere, only the external flow equations were solved. The governing equations and boundary conditions are given in *nondimensional* form using the droplet radius r_0 as the characteristic length, $\Omega_0 r_0$ as the characteristic velocity, $1/\Omega_0$ as the characteristic time, and $\rho_g(\Omega_0 r_0)^2$ and $\rho_l(\Omega_0 r_0)^2$ as the characteristic pressures for the gas and liquid phases, respectively.

Notation

c_p	specific heat
k	heat conductivity
M	dimensionless torque, Equation 25
Nu	Nusselt number
P_g	dimensionless gas pressure, normalized with respect to $\rho_g(\Omega_0 r_0)^2$
P_l	dimensionless liquid pressure, normalized with respect to $\rho_l(\Omega_0 r_0)^2$
Pr_g	gas-phase Prandtl number, $\mu_g c_{p,g}/k_g$
Pr_l	liquid-phase Prandtl number, $\mu_l c_{p,l}/k_l$
r	dimensionless radial coordinate, normalized with respect to r_0
r_0	droplet/sphere radius
Re_g	rotational gas Reynolds number, $\rho_g \Omega_0 r_0^2/\mu_g$
Re_l	rotational liquid Reynolds number, $\rho_l \Omega_0 r_0^2/\mu_l$
t	dimensional time
T	temperature
v	velocity, normalized with respect to $\Omega_0 r_0$
x	axis of rotation

Greek

γ	$-\mathrm{d}\sigma/\mathrm{d}T$
θ	polar coordinate (collatitude)
μ	dynamic viscosity
ρ	density
σ	surface tension coefficient
τ	dimensionless time; normalized with respect to $1/\Omega_0$
τ_c	characteristic deceleration time
φ	azimuthal coordinate
Ω	angular velocity

Subscripts

c	characteristic; also critical
g	gas
l	liquid
r	radial; also reference
s	droplet interface
θ	polar
φ	azimuthal
0	initial
∞	infinity

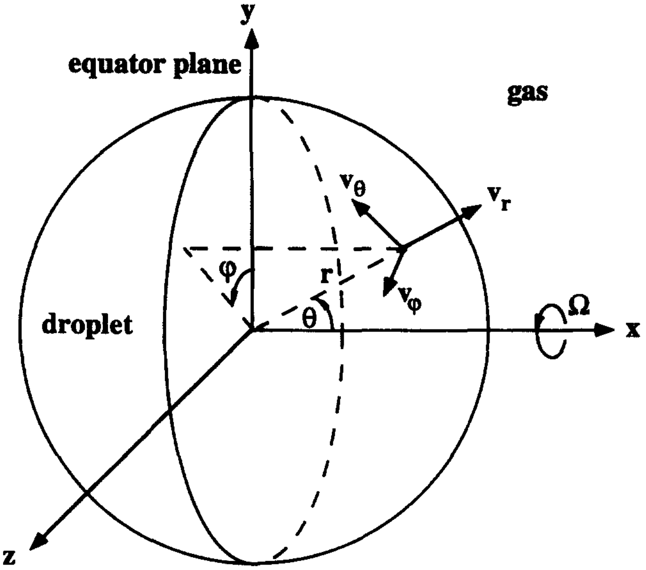

Figure 1 Schematic of rotational flow configuration; the spherical coordinate system (r, θ, ϕ) employed in the formulation is displayed; the axis of rotation coincides with the x-axis

Governing equations (in spherical coordinates)

- *Gas phase*:

continuity:

$$\frac{1}{r^2}\frac{\partial}{\partial r}(r^2 v_{r,g}) + \frac{1}{r\sin\theta}\frac{\partial}{\partial\theta}(v_{\theta,g}\sin\theta) = 0 \tag{1}$$

r-*momentum*:

$$\begin{aligned}\frac{\partial v_{r,g}}{\partial\tau} + v_{r,g}\frac{\partial v_{r,g}}{\partial r} + \frac{v_{\theta,g}}{r}\frac{\partial v_{r,g}}{\partial\theta} - \frac{v_{\theta,g}^2 + v_{\varphi,g}^2}{r} &= -\frac{\partial P_g}{\partial r} + \frac{1}{\mathrm{Re}_g}\frac{1}{r^2}\left[\frac{\partial}{\partial r}\left(r^2\frac{\partial v_{r,g}}{\partial r}\right)\right.\\ &\left.+\frac{1}{\sin\theta}\frac{\partial}{\partial\theta}\left(\sin\theta\frac{\partial v_{r,g}}{\partial\theta}\right) - 2v_{r,g} - 2\frac{\partial v_{\theta,g}}{\partial\theta} - 2v_{\theta,g}\cot\theta\right]\end{aligned} \tag{2}$$

θ-*momentum*:

$$\begin{aligned}\frac{\partial v_{\theta,g}}{\partial\tau} + v_{r,g}\frac{\partial v_{\theta,g}}{\partial r} + \frac{v_{\theta,g}}{r}\frac{\partial v_{\theta,g}}{\partial\theta} + \frac{v_{r,g}v_{\theta,g} - v_{\varphi,g}^2\cot\theta}{r} &= -\frac{1}{r}\frac{\partial P_g}{\partial\theta} + \frac{1}{\mathrm{Re}_g}\frac{1}{r^2}\left[\frac{\partial}{\partial r}\left(r^2\frac{\partial v_{\theta,g}}{\partial r}\right)\right.\\ &\left.+\frac{1}{\sin\theta}\frac{\partial}{\partial\theta}\left(\sin\theta\frac{\partial v_{\theta,g}}{\partial\theta}\right) + 2\frac{\partial v_{r,g}}{\partial\theta} - \frac{v_{\theta,g}}{\sin^2\theta}\right]\end{aligned} \tag{3}$$

φ-*momentum*:

$$\begin{aligned}\frac{\partial v_{\varphi,g}}{\partial\tau} + v_{r,g}\frac{\partial v_{\varphi,g}}{\partial r} + \frac{v_{\theta,g}}{r}\frac{\partial v_{\varphi,g}}{\partial\theta} + \frac{v_{r,g}v_{\varphi,g} + v_{\theta,g}v_{\varphi,g}\cot\theta}{r} &= \frac{1}{\mathrm{Re}_g}\frac{1}{r^2}\left[\frac{\partial}{\partial r}\left(r^2\frac{\partial v_{\varphi,g}}{\partial r}\right) + \frac{1}{\sin\theta}\frac{\partial}{\partial\theta}\left(\sin\theta\frac{\partial v_{\varphi,g}}{\partial\theta}\right) - \frac{v_{\varphi,g}}{\sin^2\theta}\right]\end{aligned} \tag{4}$$

energy:

$$\begin{aligned}\frac{\partial T_g}{\partial\tau} + v_{r,g}\frac{\partial T_g}{\partial r} + \frac{v_{\theta,g}}{r}\frac{\partial T_g}{\partial\theta} &= \frac{1}{\mathrm{Re}_g\mathrm{Pr}_g}\frac{1}{r^2}\left[\frac{\partial}{\partial r}\left(r^2\frac{\partial T_g}{\partial r}\right)\right.\\ &\left.+\frac{1}{\sin\theta}\frac{\partial}{\partial\theta}\left(\sin\theta\frac{\partial T_g}{\partial\theta}\right)\right]\end{aligned} \tag{5}$$

- *Liquid phase*:

continuity:

$$\frac{1}{r^2}\frac{\partial}{\partial r}(r^2 v_{r,l}) + \frac{1}{r\sin\theta}\frac{\partial}{\partial\theta}(v_{\theta,l}\sin\theta) = 0 \tag{6}$$

r-*momentum*:

$$\begin{aligned}\frac{\partial v_{r,l}}{\partial\tau} + v_{r,l}\frac{\partial v_{r,l}}{\partial r} + \frac{v_{\theta,l}}{r}\frac{\partial v_{r,l}}{\partial\theta} - \frac{v_{\theta,l}^2 + v_{\varphi,l}^2}{r} &= -\frac{\partial P_l}{\partial r} + \frac{1}{\mathrm{Re}_l}\frac{1}{r^2}\left[\frac{\partial}{\partial r}\left(r^2\frac{\partial v_{r,l}}{\partial r}\right)\right.\\ &\left.+\frac{1}{\sin\theta}\frac{\partial}{\partial\theta}\left(\sin\theta\frac{\partial v_{r,l}}{\partial\theta}\right) - 2v_{r,l} - 2\frac{\partial v_{\theta,l}}{\partial\theta} - 2v_{\theta,l}\cot\theta\right]\end{aligned} \tag{7}$$

θ-*momentum*:

$$\begin{aligned}\frac{\partial v_{\theta,l}}{\partial\tau} + v_{r,l}\frac{\partial v_{\theta,l}}{\partial r} + \frac{v_{\theta,l}}{r}\frac{\partial v_{\theta,l}}{\partial\theta} + \frac{v_{r,l}v_{\theta,l} - v_{\varphi,l}^2\cot\theta}{r} &= -\frac{1}{r}\frac{\partial P_l}{\partial\theta} + \frac{1}{\mathrm{Re}_l}\frac{1}{r^2}\left[\frac{\partial}{\partial r}\left(r^2\frac{\partial v_{\theta,l}}{\partial r}\right)\right.\\ &\left.+\frac{1}{\sin\theta}\frac{\partial}{\partial\theta}\left(\sin\theta\frac{\partial v_{\theta,l}}{\partial\theta}\right) + 2\frac{\partial v_{r,l}}{\partial\theta} - \frac{v_{\theta,l}}{\sin^2\theta}\right]\end{aligned} \tag{8}$$

φ-*momentum*:

$$\begin{aligned}\frac{\partial v_{\varphi,l}}{\partial\tau} + v_{r,l}\frac{\partial v_{\varphi,l}}{\partial r} + \frac{v_{\theta,l}}{r}\frac{\partial v_{\varphi,l}}{\partial\theta} + \frac{v_{r,l}v_{\varphi,l} + v_{\theta,l}v_{\varphi,l}\cot\theta}{r} &= \frac{1}{\mathrm{Re}_l}\frac{1}{r^2}\left[\frac{\partial}{\partial r}\left(r^2\frac{\partial v_{\varphi,l}}{\partial r}\right) + \frac{1}{\sin\theta}\frac{\partial}{\partial\theta}\left(\sin\theta\frac{\partial v_{\varphi,l}}{\partial\theta}\right) - \frac{v_{\varphi,l}}{\sin^2\theta}\right]\end{aligned} \tag{9}$$

energy:

$$\begin{aligned}\frac{\partial T_l}{\partial\tau} + v_{r,l}\frac{\partial T_l}{\partial r} + \frac{v_{\theta,l}}{r}\frac{\partial T_l}{\partial\theta} &= \frac{1}{\mathrm{Re}_l\mathrm{Pr}_l}\frac{1}{r^2}\left[\frac{\partial}{\partial r}\left(r^2\frac{\partial T_l}{\partial r}\right) + \frac{1}{\sin\theta}\frac{\partial}{\partial\theta}\left(\sin\theta\frac{\partial T_l}{\partial\theta}\right)\right]\end{aligned} \tag{10}$$

Boundary conditions

The conditions at the gas/droplet interface include continuity of polar and azimuthal shear stress, polar and azimuthal velocity (no slip), heat flux and temperature. No fluid is allowed to cross the liquid surface (nonevaporating droplets); therefore, the normal velocities above and below the interface are zero. The subscript s below indicates surface conditions.

$$\left(\frac{\partial v_{\theta,l}}{\partial r}-\frac{v_{\theta,l}}{r}\right)_s=\frac{\mu_g}{\mu_l}\left(\frac{\partial v_{\theta,g}}{\partial r}-\frac{v_{\theta,g}}{r}\right)_s \tag{11}$$

$$\left(\frac{\partial v_{\varphi,l}}{\partial r}-\frac{v_{\varphi,l}}{r}\right)_s=\frac{\mu_g}{\mu_l}\left(\frac{\partial v_{\varphi,g}}{\partial r}-\frac{v_{\varphi,g}}{r}\right)_s \tag{12}$$

$$v_{\theta,l,s}=v_{\theta,g,s} \tag{13}$$

$$v_{\varphi,l,s}=v_{\varphi,g,s} \tag{14}$$

$$k_l\left(\frac{\partial T_l}{\partial r}\right)_s=k_g\left(\frac{\partial T_g}{\partial r}\right)_s \tag{15}$$

$$T_{l,s}=T_{g,s} \tag{16}$$

The pressure on both sides of the droplet interface is calculated from the corresponding momentum equation in the radial direction using the most recently calculated values of the velocity field.

The liquid and gas flow boundary conditions on the rotation axis and the symmetry plane are

$$\frac{\partial P_l}{\partial\theta}=\frac{\partial v_{r,l}}{\partial\theta}=\frac{\partial T_l}{\partial\theta}=v_{\theta,l}=v_{\varphi,l}=0;\qquad \theta=0,0<r<1 \tag{17}$$

$$\frac{\partial P_l}{\partial\theta}=\frac{\partial v_{r,l}}{\partial\theta}=\frac{\partial T_l}{\partial\theta}=v_{\theta,l}=\frac{\partial v_{\varphi,l}}{\partial\theta}=0;\qquad \theta=\frac{\pi}{2},0<r<1 \tag{18}$$

$$\frac{\partial P_g}{\partial\theta}=\frac{\partial v_{r,g}}{\partial\theta}=\frac{\partial T_g}{\partial\theta}=v_{\theta,g}=v_{\varphi,g}=0;\qquad \theta=0,1<r<r_\infty \tag{19}$$

$$\frac{\partial P_g}{\partial\theta}=\frac{\partial v_{r,g}}{\partial\theta}=\frac{\partial T_g}{\partial\theta}=v_{\theta,g}=\frac{\partial v_{\varphi,g}}{\partial\theta}=0;\qquad \theta=\frac{\pi}{2},1<r<r_\infty \tag{20}$$

Finally, a zero radial flux condition ($d/dr=0$) was implemented at the outer boundary of the computational domain ($r=r_\infty$).

Initial conditions

The gas phase is initially quiescent; i.e., $v_{r,g}=v_{\theta,g}=v_{\varphi,g}=0$. The initial gas pressure and temperature are given by

$$P_g=\frac{P_0}{\rho_g(\Omega_0 r_0)^2},\qquad T_g=1000\text{ K} \tag{21}$$

where P_0 is the pressure of the undisturbed environment (one atmosphere). The liquid droplet is assumed to be initially in a rigid-body rotation around a diameter with an angular velocity Ω_0. Consequently, within the droplet

$$v_{\varphi,l}=r\sin\theta,\qquad v_{r,l}=v_{\theta,l}=0 \tag{22}$$

$$P_l=P_{l,0}+\frac{1}{2}r^2\sin^2\theta \tag{23}$$

$$T_l=280\text{ K} \tag{24}$$

where the additive function $P_{l,0}$ is determined from the initial balance of the normal stress component at the liquid–gas interface (Lozinski and Matalon 1992).

Method of solution

The solution of the system of governing equations was performed numerically using finite-difference discretization techniques. The equations were discretized spatially on a staggered mesh. Central differencing was employed for the diffusion terms, while upwind differentiation was employed for the convection terms. Forward differencing was employed in the temporal discretization. The continuity and momentum equations in which the pressure appears (i.e.; r and θ components) were solved using the time-splitting method; Ferziger (1977), Dukowicz (1980). The φ-momentum and energy equations were solved implicitly at each time step, with the most recent values used for all other field variables. The specifics of the time-splitting algorithm for this problem are given in an earlier publication (Megaridis et al. 1994).

Results and discussion

First, the accuracy of the present model is tested by considering the flow induced by a steadily rotating sphere which has been well characterized in past investigations. Subsequently, the transient gas/droplet interactions are examined in the problem of interest. Finally, the thermocapillary effect on fluid dynamics and heat transfer is discussed.

Isothermal flow induced by a steadily rotating sphere

This flow configuration involves an infinite quiescent fluid suddenly ($\tau=0$) disturbed by an impulsively started rotating sphere. A shear-induced motion is thus induced in the surrounding fluid, and as time proceeds, a steady state is approached. The transient development of the secondary (nonrotational) motion induced in the gas phase for Reynolds number 50 is shown in Figure 2 in terms of instantaneous particle pathline projections on an azimuthal plane at four different instances; $\tau=2.5$, 7.5, 15, and 25. It is apparent that the flow outside the sphere forms gradually. Early on (Figure 2A), the pathlines are tightly clustered near the sphere surface, as the shear-induced flow is confined mainly to that region. As momentum is continuously transferred from the sphere to its neighboring fluid, the closed pathlines move farther away from the sphere, and some break at the outer boundary (Figure 2B). The main feature of the ambient fluid motion is an inflow near the pole, which is balanced by an outflow along the equator. Based on Figure 2, the outflow region at the boundary near the equatorial plane becomes narrower as time proceeds. Under these conditions, it takes approximately until dimensionless time 45 for steady state to develop in the gas phase. The secondary motion at steady state is very similar to that depicted in Figure 2D.

We now consider one flow quantity which can be compared with available experimental measurements. The torque required to keep the sphere rotating at a constant angular velocity Ω in a fluid at rest has been quantified in previous papers studying this problem. Therefore, the values of torque are used to examine the grid insensitivity of the results and verify the model. The torque is normalized with respect to the quantity $(1/2)\rho_g r_0^5\Omega^2$, and its nondimensional form is

$$M=-\frac{8\pi}{\mathrm{Re}_g}\int_{\theta=0}^{\frac{\pi}{2}}\left(\frac{\partial v_{\varphi,g}}{\partial r}-\frac{v_{\varphi,g}}{r}\right)\sin^2\theta\,d\theta \tag{25}$$

with $\mathrm{Re}_g=\rho_g\Omega r_0^2/\mu_g$.

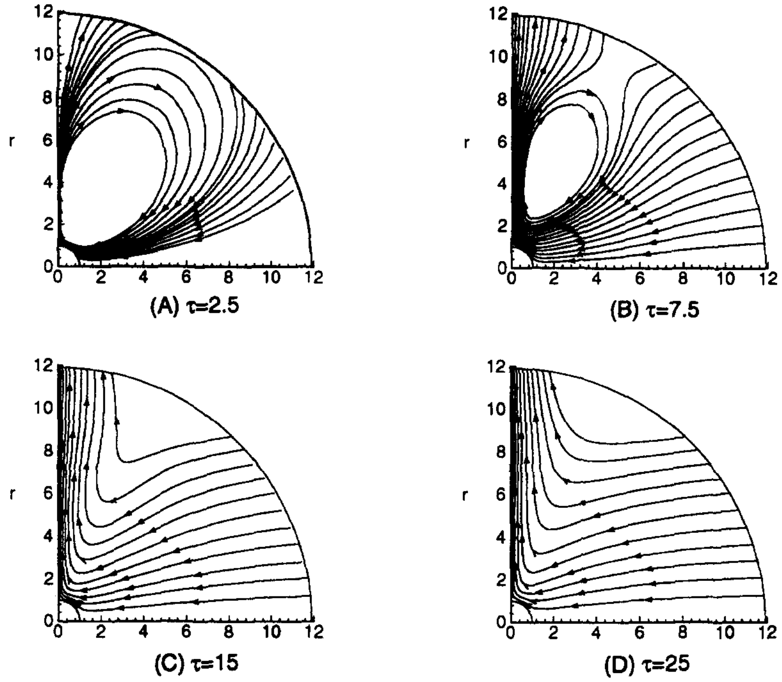

(A) τ=2.5

(B) τ=7.5

(C) τ=15

(D) τ=25

Figure 2 Transient secondary (nonrotational) motion in the gas phase as induced by a steadily rotating sphere with a Reynolds number 50; the instantaneous pathlines projected on an azimuthal plane are shown at four different instances: (A) $\tau = 2.5$, (B) $\tau = 7.5$, (C) $\tau = 15$, and (D) $\tau = 25$

Table 1 Steady state values of torque for different grids

	45 × 20	65 × 25	75 × 30
M	1.476	1.55	1.558

Numerical calculations were performed for the values of $\mathrm{Re}_g = 1$, 50, 100, 500, and 2000. The $\mathrm{Re}_g = 50$ calculations were performed for three different grids: 45 (along radial coordinate) × 20 (along polar coordinate), 65 × 25, and 75 × 30 in a spherical computational domain with an outer boundary located at twelve sphere radii from the sphere center. The location of the outer boundary was chosen after it was verified that variations of flow variables were very slow beyond ten sphere radii. Consequently, zero radial gradients were imposed on all variables at the outer boundary of the computational domain. The time-dependent solution converged asymptotically to a steady state. The calculated steady-state values of M for each of the three different grids are shown in Table 1. The dimensionless torque of the 45 × 20 grid differs by 5% from the 65 × 25 grid, while the value of M for the 75 × 30 grid differs only by 0.5% from the 65 × 25 grid. Therefore, the 65 × 25 grid was chosen to conduct the model validation comparisons with previous studies (Takagi 1977; Dennis et al. 1980, 1981; Sawatzki 1970).

The dimensionless torque at steady state is given in Table 2 for various values of Re_g. An additional quantity (θ_c; critical angle) is also given in that table. The critical angle θ_c at a specific distance from the sphere is defined as the polar coordinate where the surrounding fluid changes its direction from inflow (towards the sphere) to outflow (away from the sphere). In the comparisons of Table 2, the critical angle was determined at a distance of $1.2r_0$ from the sphere center ($0.2r_0$ from the surface). As seen in Table 2, the calculated asymptotic results show excellent agreement with previously published data over a wide range of Re_g. It is noted that due to limitations of the series method, no data for large Reynolds numbers are available in Takagi (1977) and Dennis et al. (1980).

The variation of θ_c shown in Table 2 indicates that the region of inflow increases with Re_g, thus causing a corresponding decrease of the outflow region near the equator. It should be noted that as the Reynolds number increases, the boundary layer on the sphere surface becomes thinner. Thus, it is necessary to

Table 2 Steady state values of torque and critical angle at various Reynolds numbers

		Dennis et al. (1980)				This study	
Re_g	Takagi (1977), *M*	*M*	θ_c	Dennis et al. (1981), *M*	Sawatzki (1970), *M*	*M*	θ_c
1	50.307	50.309	54.8	50.305		50.7	53.8
50		1.554	69.4	1.554	1.55	1.55	67.45
100		0.966	73.8	0.966	0.966	0.954	73.6
500				0.348	0.35	0.367	77.7
2000				0.158	0.16	0.15	80.8

choose finer mesh sizes near the sphere surface for larger values of Re_g. The 65×25 grid was used for $\mathrm{Re}_g = 1$, 50, and 100, while a grid 90×25 was used for $\mathrm{Re}_g = 500$ and 2000.

Rotationally decelerating droplets with heat transfer

In this flow configuration, a spinning droplet is suddenly placed in a hot, initially quiescent, gaseous environment. At time zero, the droplet internal motion is a solid-body rotation. Due to shear stresses on the gas/liquid interface, the rotation speed of the droplet decays gradually, while the surrounding gas is set into motion. Unlike the case of a sphere rotating with constant angular velocity (where a steady state is eventually reached in the gas), the induced gas secondary motion in the current problem achieves maximum strength, and decays thereon as the angular velocity of the droplet decreases. Meanwhile, the fluid inside the droplet is gradually heated up.

In most spray applications, the size of droplets is $O(100\ \mu\mathrm{m})$, and the typical frequency of similar size turbulent eddies is $O(100\ \mathrm{Hz})$. As a result, the corresponding gas-phase Reynolds number is small. For example, for a 200-μm diameter droplet rotating at 100 Hz in 1 atm and 1000 K air, $\mathrm{Re}_g < 0.1$. Consequently, the calculations described below focus on small values of Re_g as being representative of spray combustion applications. It should be noted that the corresponding liquid Reynolds numbers are two orders of magnitude larger than the gas Reynolds numbers. Because the Reynolds number is small in the flow configuration considered in this section, the 65×25 grid was used in the gas phase, along with the 16×25 grid in the liquid phase.

For the base case, the Reynolds number $\mathrm{Re}_g = \rho_g \Omega_0 r_0^2 / \mu_g$ was selected to be 0.41. This value corresponds to a droplet radius of 300 μm, initial rotation frequency 30 Hz, ambient temperature 1000 K, and ambient pressure 1 atm. These ambient conditions also correspond to $\mathrm{Pr}_g = 0.68$ and $\mathrm{Pr}_l = 8$. It is emphasized that the base case results in their nondimensional form are also applicable for other combinations of droplet sizes and rotation frequencies, as long as the product $\Omega_0 r_0^2$ and the ambient conditions remain unchanged. The liquid considered is n-decane, as being representative of low-volatility hydrocarbon fuels.

The transient azimuthal velocity component in both phases at $\theta = 44°$ is shown as a function of radial position in Figure 3A. The rotational velocity on the droplet surface gradually decreases, while the extent of the affected gaseous region remains nearly constant ($r < 5$). Within that region, the azimuthal gas velocity decreases monotonically in time with the exception of the very early stages during which the quiescent gas adapts to the droplet rotation. Because of the higher liquid viscosity, the azimuthal velocity profile in the droplet interior is almost linear with respect to r, which also indicates that momentum transfer in the liquid is relatively fast. Figure 3B displays the transient radial variation of the polar velocity component in both phases at $\theta = 44°$. It is seen that the strength of this component reaches its peak at $\tau = 2.4$ and then decreases gradually. Also, the polar velocities on the droplet surface remain negative, which indicates that the surface liquid moves from the equator to the pole. In contrast, the bulk gas flow is directed from the pole to the equator (see Figure 2), although the gas does move from the equator to the pole in the vicinity of the droplet surface (see Figure 3B). This trend supports the view that the secondary motion within the droplet is dominated by the deceleration mechanisms. Overall, however, the polar velocity component is small, thus suggesting that nonrotational motion in both phases is weak.

The temporal variations of the azimuthal velocity component at several representative locations in both phases are shown in Figure 4. Three of these locations (B, C, D) lie along a radius at $\theta = 45°$, with the fourth one being on the equator; $\theta = 90°$. Locations A and C are on the droplet surface. It is apparent (see curves A, B, and C) that rotational velocities in the liquid phase decrease monotonically with time. For the gas phase, the azimuthal velocity values increase early on due to the momentum transferred from the spinning droplet, reach a maximum ($\tau \sim 2.4$ at D), and then decrease steadily.

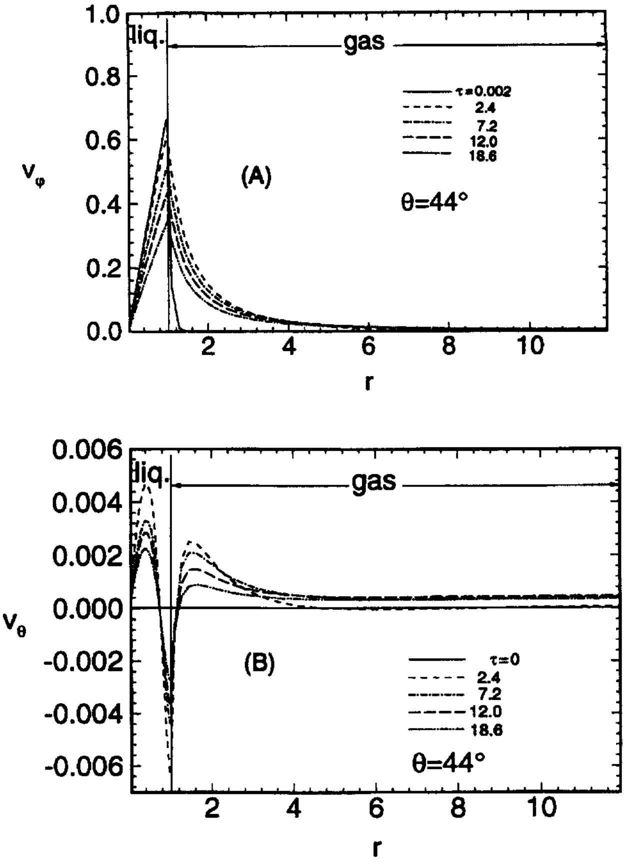

Figure 3 Transient velocity radial distributions in liquid and gas phases at $\theta = 44°$ for $\mathrm{Re}_g = 0.41$; (A) azimuthal velocity component, (B) polar velocity component

The azimuthal and polar shear stresses on the droplet surface are shown in Figure 5 (A and B, respectively). As expected, because the azimuthal direction is the primary direction of fluid motion, the corresponding shear stress is much larger than its

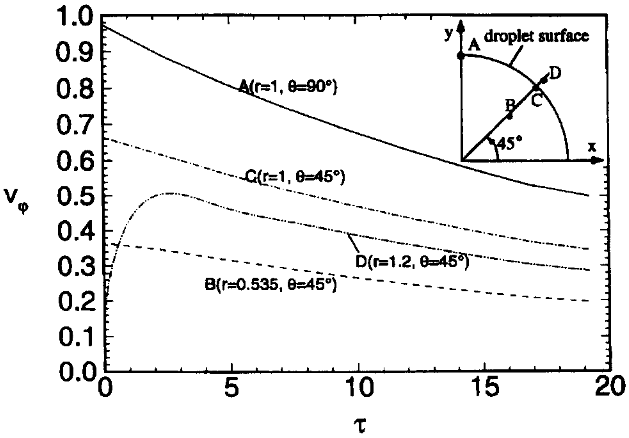

Figure 4 Temporal variations of the azimuthal velocity component at several representative locations (marked on inset) in both phases of the base case calculation; $\mathrm{Re}_g = 0.41$

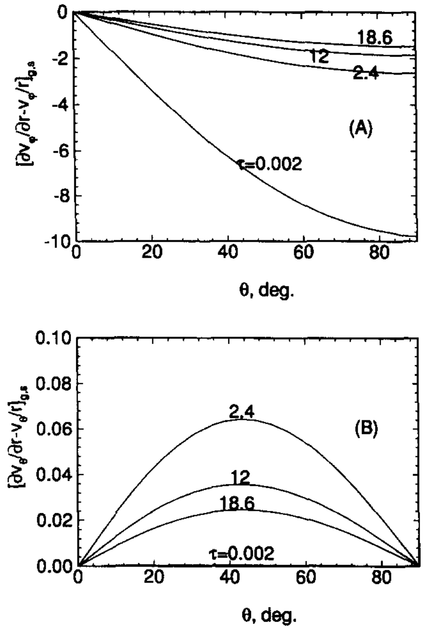

Figure 5 Transient azimuthal (A) and polar (B) shear stress variations on the gas/liquid interface for $\mathrm{Re}_g = 0.41$

polar counterpart. During the examined time period ($\tau \leq 18.6$), the former is two orders of magnitude higher than the latter. Initially, the azimuthal shear stress is very high due to the sudden exposure of the spinning droplet to the quiescent ambient gas. As momentum is transfered from the droplet to the gas and the droplet is slowed down, the azimuthal shear stress decreases monotonically in magnitude. As a consequence of the initial solid-body rotation, the polar shear stress is zero at $\tau = 0$. As the induced secondary motion develops within the gaseous environment, the polar shear stress increases and achieves a maximum at $\tau = 2.4$. Thereon, it decreases as the flow engendered in the gas phase decays.

The polar profiles of rotation frequency and azimuthal velocity component on the gas/liquid interface are illustrated in Figure 6 for three different instances of the simulation; namely, $\tau = 2.4$, 12, and 18.6. From this figure, the gradual decay of the azimuthal velocity component on the droplet surface is apparent (see $v_{\phi,s}$ curves). The local rotation frequency f_s on the droplet surface shows only weak variation with polar angle. At $\tau = 18.6$, the droplet surface has decelerated to half of its initial rotation frequency (30 Hz).

The secondary motion in the gas phase around the droplet is shown in Figure 7A in terms of instantaneous particle pathline projections on an azimuthal plane at three different instances; $\tau = 2.4$, 12, and 18.6. Similar to the ambient flow driven by a rotating solid sphere (Figure 2), the inflow at the pole is balanced by an outflow near the equator. It is also apparent that the flow region expands gradually along $\theta = 45°$ due to momentum diffusion. The secondary flow in the droplet interior is exemplified by that depicted in Figure 7B ($\tau = 12$). Due to viscous shear stresses on the interface, the droplet-surface rotation speed is reduced gradually, and the pressure balance with the centrifugal forces is disturbed. The clockwise direction of the secondary flow in the droplet interior suggests that this motion is dominated by the liquid deceleration mechanisms. It is noted that the projected motion seen in Figure 7B is superimposed on the primary rotational (azimuthal) motion. Thus, a typical liquid element starting near the equatorial plane below the droplet surface follows a spiraling motion towards the pole along this surface and spirals inward from the pole to the droplet center. Subsequently, this liquid element turns away from the axis of rotation and winds around this axis until it reaches its original position near the droplet surface. The droplet internal circulation described above is very similar to that visualized by Wimmer (1988) who examined experimentally unsteady liquid flows within rotating spheres. This internal flow pattern also resembles the one determined analytically by Lozinski and Matalon (1993). However, the qualitatively similar motion reported in the work of Lozinski and Matalon (1993) is due to thermocapillary forces established on the nonisothermal surface of a droplet rotated in a rigid-body fashion. Finally, the droplet internal circulation during spindown as seen in this study is similar to that induced by spatially nonuniform but steady surface rotation (Megaridis et al. 1994). The nonrotational motion seen in Figure 7 for both phases may influence heat transport, which, in turn, can affect evaporation rates.

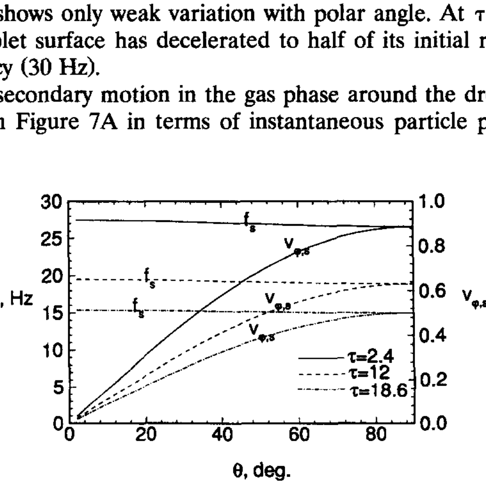

Figure 6 Polar profiles of rotation frequency and azimuthal velocity component on the gas/liquid interface for three different instances of the base case simulation; $\tau = 2.4$, 12, and 18.6.

Transient heat transfer in rotational flows has been studied by Kreith et al. (1963) who used small metal spheres and considered uniform temperature distribution in the solid. The transient temperature variations along r at $\theta = 90°$ are shown in Figure 8 for the base case calculation. The displayed profiles are representative of those at other polar angles as well, and clearly demonstrate a nonuniform temperature distribution in both phases. As expected, the droplet is heated up from its surface to the core, while the gas is cooled down in the vicinity of the droplet. The diminishing radial gradients of temperature above the gas/droplet interface suggest that the heat flux to the droplet interior decreases with time. The temperature fields in the entire domain are shown in Figure 9. The isotherms in the gas (Figure 9A) maintain a nearly concentric circle shape, thus indicating that heat transfer along the radial coordinate in the gas phase is dominated by heat conduction. Within the droplet (Figure 9B), heat conduction is again the main mechanism of heat transfer along r. The effect of the induced secondary motion on heat transfer in both phases appears to be negligible under the base case conditions.

The surface-average Nusselt number is expressed as

$$\overline{\mathrm{Nu}} = \frac{2k_l \int_{\theta=0}^{\pi} \left(\frac{\partial T_l}{\partial r}\right)_s \sin\theta \, d\theta}{k_g (T_{g,\infty} - T_{l,s,\mathrm{av}})} \tag{26}$$

where the subscript av indicates surface-averaged value. The temporal variation of $\overline{\mathrm{Nu}}$ for the base case is shown in Figure 10. With the exception of the early stages, the average Nusselt number is almost constant, and very close to the value of 2, consistent with Stokes's theory (White 1991). This result confirms that the swirling flow in the base case droplet has negligible impact on heat transfer.

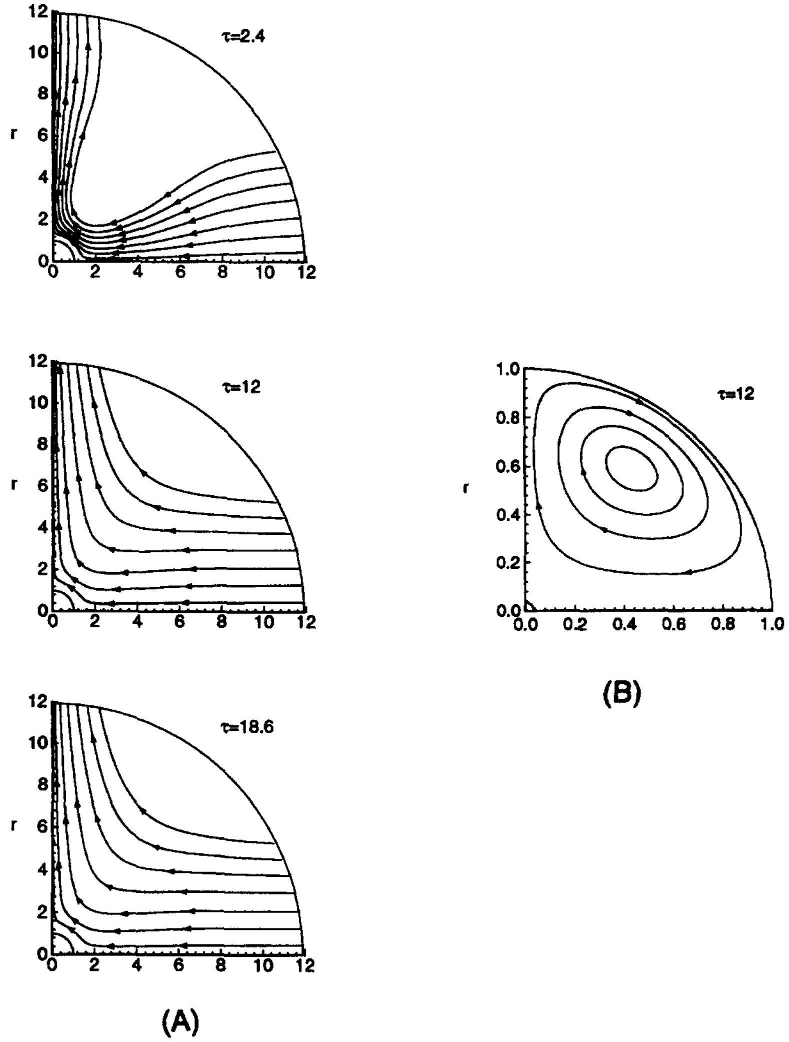

Figure 7 Transient secondary motion for $\mathrm{Re}_g = 0.41$; (A) gas phase at $\tau = 2.4$, 12, and 18.6, (B) liquid phase at $\tau = 12$; instantaneous particle pathline projections on an azimuthal plane are shown; note that this motion is superimposed on the primary rotation

The influence of $\mathrm{Re}_g = r_0^2\Omega_0\rho_g/\mu_g$ on the strength of the induced secondary motion was examined. The base case value of $r_0^2\Omega_0$ was modified to obtain a range of values for Re_g. All other parameters were identical to those considered in the base case simulation. The azimuthal and polar shear stress distributions along θ are shown in Figure 11 for $\mathrm{Re}_g = 0.045$, 0.41, 4.5, and 18.1. The shown distributions correspond to the instant (in each simulation) where the azimuthal rotation frequency at the equator has dropped to 50% of its initial value. This instant defines the characteristic deceleration time τ_c, which is used in the following to quantify droplet deceleration behavior. As seen in Figure 11A, the azimuthal shear stress distribution changes slightly with Re_g. In contrast, the polar shear stress (Figure 11B) changes dramatically and increases monotonically with Reynolds number. The results demonstrate that the secondary motion is strengthened at increased Re_g.

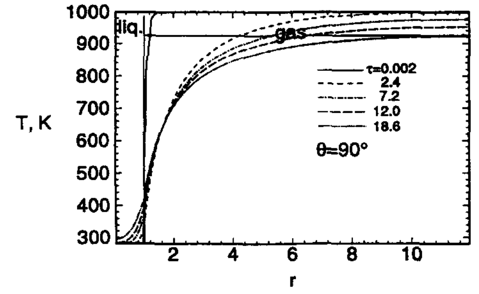

Figure 8 Transient temperature radial profiles at $\theta = 90°$ in both phases for the base case calculation; $\mathrm{Re}_g = 0.41$

Figure 12 presents the characteristic deceleration time versus initial Reynolds number and shows that τ_c is linearly dependent on Re_g. If the initial rotating frequency is constant, from the definition of the Reynolds number it is deduced that τ_c is proportional to the square of the droplet radius. It is known that the characteristic deceleration time depends on the friction torque acting on the interface as well as on the initial kinetic energy of the droplet. In fact, τ_c is expected to be proportional to kinetic energy and inversely proportional to friction torque. From Equation (25) and the fact that the dimensional torque is normalized with respect to $(1/2)\rho_g r_0^5\Omega_0^2$, one deduces that, for the same initial rotating frequency, the dimensional torque is proportional to the cube of the droplet radius and the integral of azimuthal shear stress on the interface. As seen in Figure 11A, the induced secondary motion does not have significant effects

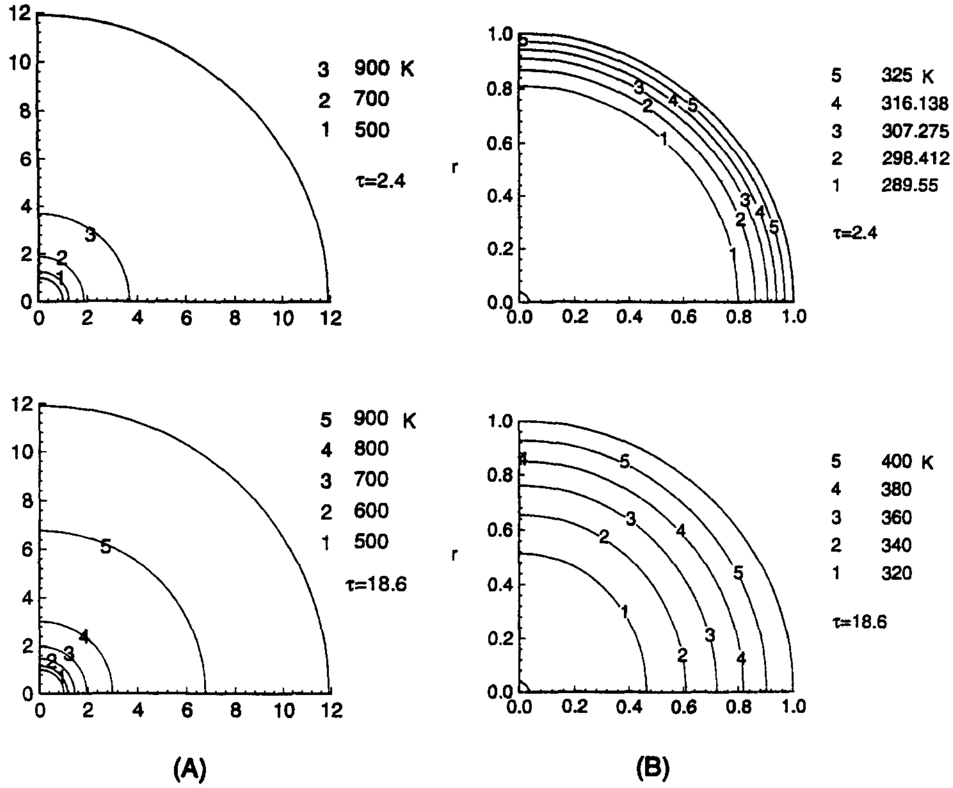

Figure 9 Temperature contours in gas (A) and liquid phases (B) for $Re_g = 0.41$ at $\tau = 2.4$, and $\tau = 18.6$

on azimuthal velocity distribution, and the azimuthal shear stresses for various Reynolds numbers do not change by much. Therefore, the dimensional torque is proportional to the cube of the droplet radius. On the other hand, the kinetic energy of the rotating droplet is proportional to the fifth power of the droplet radius for the same initial rotating frequency. From the above physical arguments applied for constant initial rotation frequency, it is apparent why the characteristic deceleration time τ_c increases in linear proportion to the square of the droplet radius, and in turn, to the rotational Reynolds number (Figure 12).

For constant droplet size and unchanged ambient conditions, the values of Re_g can be modified by adjusting the droplet rotation speed. In that case, both Reynolds number and nondimensional time are proportional to the initial rotation velocity; therefore, the linearity of τ_c with Re_g (Figure 12) is expected. Furthermore, the linear τ_c *versus* Re_g behavior also suggests that the dimensional characteristic deceleration time t_c for constant

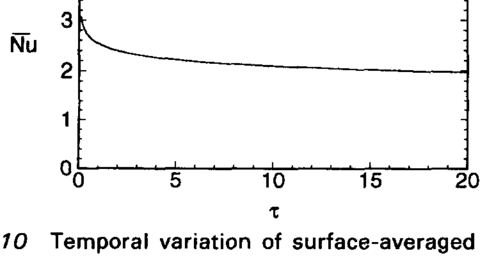

Figure 10 Temporal variation of surface-averaged Nusselt number $\overline{Nu}$ for the base case calculation

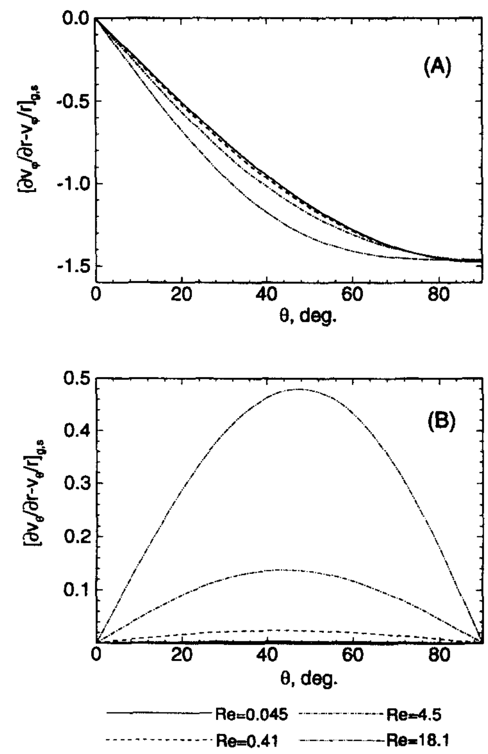

Figure 11 Transient azimuthal (A) and polar (B) shear stress distributions along θ for $Re_g = 0.045$, 0.41, 4.5, and 18.1; the shown distributions correspond to the instant (in each simulation) where the azimuthal rotation frequency at the equator has dropped to 50% of its initial value

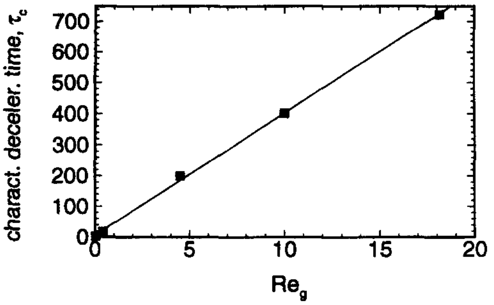

Figure 12 Nondimensional characteristic droplet deceleration time versus initial Reynolds number

droplet size does not vary with rotation speed (or Reynolds number) within the Reynolds number range considered herein.

The linear τ_c *versus* Re_g (or $t_c\Omega_0$ vs. $r_0^2\Omega_0\rho_g/\mu_g$) behavior of Figure 12 infers that the dimensional characteristic deceleration time t_c is proportional to the square of the droplet radius. The empirical relation between the droplet radius (r_0, m) and the dimensional characteristic deceleration time (t_c, seconds) was obtained as $t_c = 1.11 \times 10^6 r_0^2$, where the proportionality coefficient was determined by averaging six cases within the droplet size range from 25 μm to 2000 μm and ambient conditions of 1000 K and 1 atm.

Let us now consider a droplet radius of 100 μm and an initial spinning frequency of 30 Hz, as values typical of spray combustion applications. For an ambient of 1000 K, 1 atm, and an initial droplet temperature of 280 K, the model predicted a dimensionless characteristic time $\tau_c = 2.1$ for 50% rotational deceleration. At that instant, the average droplet-surface temperature was 422 K, which is lower than the wet bulb temperature of compounds in Diesel oil and heavy oil fuels. Thus, the numerical results indicate that the rotational deceleration process lasts for the entire liquid heating period which persists over a good portion of the droplet evaporation lifetime. Sirignano (1983) reported that for fuel droplets of practical interest (25 μm and up), the time for velocity relaxation due to drag is comparable or greater than the droplet lifetime. It is, therefore, anticipated that under the conditions considered herein, the droplet rotational deceleration time and the translational relaxation time due to drag are comparable. This was verified by performing an additional calculation to estimate the response time of a translationally moving droplet. The approach of Chin and Lefebvre (1985) for single-droplet evaporation in a convective field was followed. In this calculation, the initial n-decane droplet velocity, temperature and radius were 20 m/s, 280 K, and 100 μm, respectively. The surrounding quiescent gas-phase conditions were 1 atm and 1000 K. It was found that the droplet decelerated to half of its initial translational velocity (10 m/s) in 0.011 s, or 2.1 (normalized by $1/\Omega_0$; i.e., $1/60\pi$). Consequently, both rotational and translational deceleration can co-exist during a large portion of the transient droplet heatup period and should be considered simultaneously in spray calculations involving rotation superimposed on translation.

Thermocapillary flow effects

The droplet temperature distributions displayed in Figure 9B are representative of rotational configurations relevant to spray combustion at atmospheric pressure; $\mathrm{Re}_g = O(0.1)$. As stated previously, the radial heat transport under these circumstances is dominated by conduction and the temperature along the gas/liquid interface is practically uniform. To this end, thermocapillary terms in the droplet-surface stress balance can be safely neglected. However, larger values of the rotational Reynolds number induce stronger secondary motion (Figure 11B) which is capable of causing appreciable temperature gradients along the gas/liquid interface, and in turn, triggering thermocapillary motion.

Steady-state droplet thermocapillary flows have been studied theoretically by Jayaraj et al. (1981) as well as by Lozinski and Matalon (1993). In Jayaraj et al., the induced secondary motion within a nonrotating and nonvaporizing droplet was examined by imposing a prescribed temperature distribution on the droplet surface. Lozinski and Matalon (1993), on the other hand, used analytical methods to study thermocapillary motion in a spinning vaporizing droplet under conditions of weak rotation.

When the thermocapillary effect is taken into account, all governing equations describing the flow of Figure 1 are identical to those given in the previous section, except for the polar shear stress balance given by Equation 11. The temperature dependence of the surface tension coefficient σ of a liquid is expressed by

$$\sigma = \sigma_r - \gamma(T - T_r) \tag{27}$$

where σ_r is the value at the reference temperature T_r, and γ defines the sensitivity of σ to temperature ($\gamma = -d\sigma/dT$). In this study, a constant value of $\gamma = 10^{-4}$ N/mK was used, as being representative of most hydrocarbon fuels (Vargaftik 1975). Because the secondary motion affects the temperature distribution only along the polar coordinate of the droplet surface, the corresponding shear stress balance equation becomes

$$\mu_l\left[\frac{\partial v_{\theta,l}}{\partial r} - \frac{v_{\theta,l}}{r}\right]_s = \mu_g\left[\frac{\partial v_{\theta,g}}{\partial r} - \frac{v_{\theta,g}}{r}\right]_s - \frac{\gamma}{\Omega_0 r_0}\frac{\partial T_s}{\partial \theta} \tag{28}$$

Equation 28 shows that surface tension variation due to temperature nonuniformity on the interface drives the flow from hot to cool regions (Marangoni flow). In the present investigation, the droplet shape is assumed to remain spherical, and, thus, the normal stress balance at the surface is ignored.

Millimeter-sized droplets are frequently used in laboratory experiments. Because such droplets (when rotating) are associated with larger values of Re_g, it is expected that the thermocapillary effect may be more significant in these cases. The numerical simulations described in the following correspond to a relatively large droplet compared with droplet sizes representative of practical spray combustion applications. The droplet has a radius of 2 mm, and initially rotates around its diameter at 30 Hz. All other conditions are the same as those considered in the base case calculation. The initial rotational Reynolds number Re_g is 18. This calculation was pursued up to $\tau = 820$, when the liquid-phase temperatures became high enough to render the nonevaporation assumption invalid.

A comparison is conducted below between the model predictions when the surface tension gradients are taken into account ($\gamma = 10^{-4}$ N/mK) and when they are neglected ($\gamma = 0$). Figure 13 shows the temperature distributions on the droplet surface along θ for both cases at $\tau = 96$ and $\tau = 336$. When neglecting thermocapillary effects ($\gamma = 0$), the droplet surface temperature decreases monotonically from the pole ($\theta = 0$) to the equator ($\theta = 90°$). The induced gas swirling flow brings hot air towards the pole along the axis of rotation (Figure 7A), and, consequently, the heat flux from the gas to the liquid is higher near the pole. It is noteworthy that the droplet-surface temperature difference increases as time proceeds; compare the curve at $\tau = 96$ with that at $\tau = 336$ in Figure 13. Figure 13 also shows that the droplet-surface temperature profiles for $\gamma = 10^{-4}$ N/mK

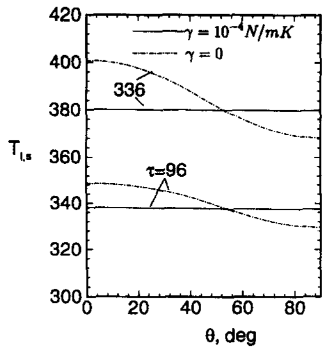

Figure 13 Comparison of droplet-surface temperature distributions along θ for $Re_g = 18$; curves with and without thermocapillary stresses ($\gamma = 10^{-4}$ N/mK, $\gamma = 0$, respectively) are shown at $\tau = 96$ and 336

are much flatter than those with $\gamma = 0$. The temperature-induced thermocapillary stress results in fluid motion on the droplet surface from the pole to the equator, thus enhancing heat transfer along θ, and in turn, making the droplet-surface temperature distribution more uniform (see solid curves in Figure 13).

Figure 14 shows polar velocity profiles on the droplet surface at three different instances ($\tau = 96$, 336 and 672) of the calculations with $\gamma = 10^{-4}$ N/mK and $\gamma = 0$. The polar velocities for $\gamma = 10^{-4}$ N/mK are by one order of magnitude higher than those for $\gamma = 0$. The significant increase in these velocities is attributed to the influence of thermocapillary stresses. Although thermocapillary motion was found to increase droplet-surface polar velocities significantly, the dominant mechanism of heat transfer within the droplet was still heat conduction. On the other hand, the swirling flow in the gas phase for $Re_g = 18$, $\gamma = 10^{-4}$ N/mK was found to enhance heat transfer; see isotherms in Figure 15A and compare with those of Figure 9A ($Re_g = 0.41$, $\gamma = 0$). Thus, it is concluded that the induced secondary motion in the gas becomes important as the rotational Reynolds number increases. Figure 15B depicts the secondary motion in the liquid phase in terms of instantaneous particle pathline projections on an azimuthal plane at an instant $\tau = 144$. The influence of both dynamic spindown and thermocapillary stresses is demonstrated by the two counterrotating flow structures; the one near the droplet surface is driven by thermocapillary stresses, while the other closer to the core of the droplet is dominated by the convective spindown mechanisms. When the rotating droplet is suddenly exposed to the hot ambient, the temperature on the droplet surface near the pole (θ = 0°) is higher than that near the equator (θ = 90°); see Figure 13. This triggers thermocapillary motion on the droplet interface driving fluid parcels from the pole to the equator, thus enhancing the convective heat transport on the droplet surface, and in turn, causing more uniform temperature distribution (see Figure 13). Although the polar temperature gradients are eliminated early on by this action, the thermocapillary motion does not disappear immediately because of the fluid inertial forces.

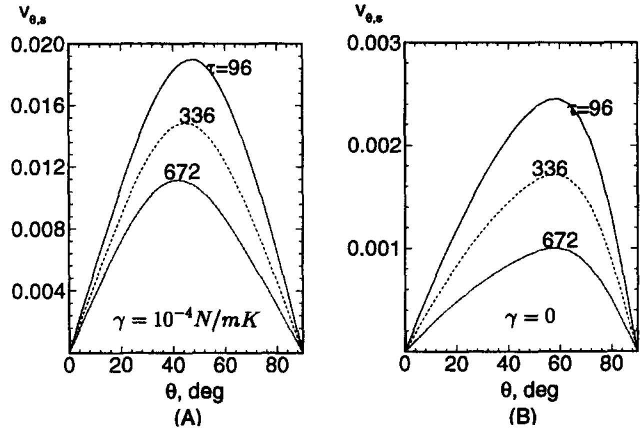

Figure 14 Polar velocity profiles on the droplet surface at three different instances ($\tau = 96$, 336, and 672) of the calculations with (A) $\gamma = 10^{-4}$ N/mK and (B) $\gamma = 0$

Conclusions

A modeling study of the spindown flow induced when a rotating droplet is suddenly exposed to an initially undisturbed infinite fluid has been conducted. The droplet enters the hot gas rotating about a central axis and has no translational motion with respect to the suspending medium. The coupled unsteady Navier–Stokes and energy equations were solved using finite-difference discretization techniques and a numerical solution procedure. The model was verified first by considering a rotating solid-sphere configuration which has been studied extensively in the past.

The model predictions showed that helical internal flows appear within a rotating droplet during spindown. A freely decelerating droplet induces a nonrotational motion to the surrounding gas, which is drawn towards the pole and directed outwards along the equator plane. The Reynolds number has significant effects on the strength of the secondary (nonrotational) motion. For droplet sizes and rotation frequencies representative of droplet combustion applications; i.e., Reynolds ~$O(0.1)$, the secondary motion in both phases remains weak, and heat trans-

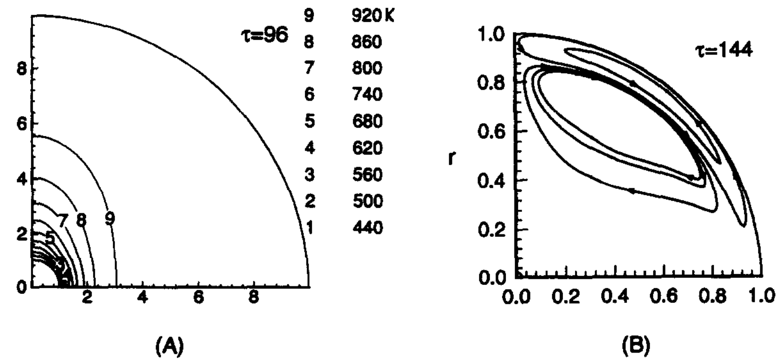

Figure 15 (A) Instantaneous thermal field in gas phase at $\tau = 96$; (B) secondary motion in the liquid phase in terms of instantaneous particle pathline projections on an azimuthal plane at $\tau = 144$; both frames correspond to $Re_g = 18$ and $\gamma = 10^{-4}$ N/mK

port is conduction-dominated. On the other hand, at increased values of the rotational Reynolds number, the secondary motion is strengthened and affects energy transport in both phases. The characteristic time for droplet spindown was found to be proportional to the square of droplet radius and independent of the initial rotation frequency. The simulations also showed that the characteristic time for rotational deceleration is of the same order of magnitude with the estimated translational response time of a droplet. Consequently, both rotational and translational deceleration can co-exist during a large portion of the transient droplet heatup period and should be considered simultaneously in spray calculations involving rotation and translation. Finally, thermocapillary stresses were found to smear temperature gradients on the droplet surface for large rotational Reynolds numbers; $O(10)$. At these conditions, the Marangoni stresses have significant impact on the fluid dynamical and heat transport processes and, thus, cannot be neglected.

Acknowledgments

Useful discussions with Joseph Hodges and Cary Presser of NIST are acknowledged with appreciation. The support of the Pittsburgh Supercomputing Center through an allocation of computer time on the Cray C-90 is also acknowledged.

References

Banks, W. H. H. 1976. The laminar boundary layer on a rotating sphere. *Acta Mech.*, **24**, 273–287

Chin, J. S. and Lefebvre, A. H. 1985. The role of the heat-up period in fuel drop evaporation. *Int. J. Turbo Jet Engines*, **2**, 315–325

Collins, W. D. 1955. On the steady rotation of a sphere in a viscous fluid. *Mathematika*, **2**, 42

Dennis, S. C. R. and Ingham, D. B. 1979. Laminar boundary layer on an impulsively started rotating sphere. *Phys. Fluids*, **22**, 1–9

Dennis, S. C. R., Singh, S. N. and Ingham, D. B. 1980. The steady flow due to a rotating sphere at low and moderate Reynolds numbers. *J. Fluid Mech.*, **101**, 257–279

Dennis, S. C. R., Ingham, D. B. and Singh, S. N. 1981. The steady flow of a viscous fluid due to a rotating sphere. *Quart. J. Mech. Appl. Math.*, **24**, 361–381

Dukowicz, J. K. 1980. A particle-fluid numerical model for liquid sprays. *J. Comp. Physics*, **35**, 229–253

Dwyer, H. D. 1989. Calculations of droplet dynamics in high temperature environments. *Prog. Energy Combust. Sci.*, **15**, 131–158

Faeth, G. M. 1983. Evaporation and combustion of sprays. *Prog. Energy Combust. Sci.*, **9**, 1–76

Ferziger, J. H. 1977. Large eddy numerical simulations of turbulent flows. *AIAA J.*, **15**, 1261–1267

Howarth, F. R. S. 1951. Note on the boundary layer on a rotating sphere. *Phil. Mag.*, **42**, 1308–1315

Hou, S. S., and Lin, T. H. 1993. A liquid-pool simulation of droplet combustion in a swirl flow. *J. Energy Resources Technol.* **115**, 175–182

Jayaraj, K., Cole, R. and Shankar Subramanian, R. 1981. Combined thermocapillary and buoyant flow in a drop in a space laboratory. *J. Colloid Interface Sci.*, **85**, 66–77

Kobashi, Y. 1957. Measurements of boundary layer of a rotating sphere. *J. Sci.* (Hiroshima Univ.), **A 20**, 149

Kohama, Y. and Kobayashi, R. 1983. Boundary-layer transition and the behaviour of spiral vortices on rotating spheres. *J. Fluid Mech.*, **137**, 153–164

Kreith, F., Roberts, L. G., Sullivan, J. A. and Sinha, S. N. 1963. Convection heat transfer and flow phenomena of rotating spheres. *Int. J. Heat Mass Transfer*, **6**, 881–895

Law, C. K. 1982. Recent advances in droplet vaporization and combustion. *Prog. Energy Combust. Sci.*, **8**, 171–201

Lozinski, D. and Matalon, M. 1992. Vaporization of a spinning fuel droplet. *Proc. 24th Int. Symposium on Combustion*, The Combustion Institute, 1483–1491

Lozinski, D. and Matalon, M. 1993. Thermocapillary motion in a spinning vaporizing droplet. *Phys. Fluids A*, **5**, 1596–1601

Lozinski, D. and Matalon, M. 1994. Combustion of a spinning fuel droplet. *Combust. Sci. Technol.*, **96**, 345–367

Megaridis, C. M., Hodges, J. T., Xin, J., Day, J. M. and Presser, C. 1994. Internal droplet circulation induced by surface-driven rotation. *Int. J. Heat Fluid Flow*, **15**, 364–377

Nigam, S. D. 1954. Note on the boundary layer on a rotating sphere. *Z. Angew. Math. Phys.* **5**, 151–154

Pearlman, H. G. and Sohrab, S. H. 1991. The role of droplet rotation in turbulent spray combustion modelling. *Combust. Sci. Technol.*, **76**, 321–334

Sawatzki, O. 1970. Das Stromungsfeld um eine rotierende Kugel, *Acta Mech.*, **9**, 159–214

Sirignano, W. A. 1983. Fuel droplet vaporization and spray combustion theory. *Prog. Energy Combust. Sci.*, **9**, 291–332

Sirignano, W. A. 1993. Fluid dynamics of sprays—1992 Freeman Scholar Lecture. *J. Fluids Eng.*, **115**, 345–378

Stokes, G. G. 1845. On the theories of the intern friction of fluids in motion. *Camb. Trans.*, **8**, 287

Takagi, H. 1977. The laminar incompressible boundary layer on a rotating sphere. *J. Phys. Soc. Japan*, **42**, 319

Tennekes, H. and Lumley, J. L. 1972. *A First Course in Turbulence*. The MIT Press, Cambridge, MA, 2, 3

Thomas, R. H. and Walters, K. 1964. The motion of an elasticoviscous liquid due to a sphere rotating about its diameter. *Quart. J. Mech. Appl. Math.*, **17**, 39

Vargaftik, N. B. 1983. *Handbook of Physical Properties of Liquids and Gases*. Hemisphere, Washington, DC, 273

White, F. M. 1991. *Viscous Fluid Flow*, 2nd ed. McGraw-Hill, New York

Wimmer, M. 1988. Viscous flows and instabilities near rotating bodies. *Prog. Aerospace Sci.*, **25**, 43–103

Xin, J. and Megaridis, C. M. 1996. Effects of rotating gaseous flows on transient droplet dynamics and heating. *Int. J. Heat Fluid Flow*, **17**, 52–62